Acta Crystallographica Section B
Structural Science, Crystal Engineering and Materials
ISSN 2052-5206

Spin Reorientation and the Interplay of Magnetic Sublattices in $Er_2CuMnMn_4O_{12}$

John M. Attah-Baah,[a,b] Dmitry D. Khalyavin,[c] Pascal Manuel,[c] Nilson S. Ferreira,[b] Alexei A. Belik[d] and Roger D. Johnson [a,e,f]*

[a]Department of Physics and Astronomy, University College London, Gower Street, London WC1E 6BT, United Kingdom, [b]Department of Physics, Federal University of Sergipe, São Cristovão 49100-000, SE Brazil, [c]ISIS facility, Rutherford Appleton Laboratory-STFC, Chilton, Didcot OX11 0QX, United Kingdom, [d]Research Center for Materials Nanoarchitectonics (MANA), National Institute for Materials Science (NIMS), 1-1 Namiki, Tsukuba, Ibaraki 305-0044, Japan, [e]London Centre for Nanotechnology, University College London, Gower Street, London WC1E 6BT, United Kingdom, and [f]Diamond Light Source, Rutherford Appleton Laboratory-STFC, Chilton, Didcot OX11 0QX, United Kingdom. Correspondence e-mail: roger.johnson@ucl.ac.uk

Through a combination of magnetic susceptibility, specific heat, and neutron powder diffraction measurements we have revealed a sequence of 4 magnetic phase transitions in the columnar quadruple perovskite $Er_2CuMnMn_4O_{12}$. A key feature of the quadruple perovskite structural framework is the complex interplay of multiple magnetic sublattices via frustrated exchange topologies and competing magnetic anisotropies. We show that in $Er_2CuMnMn_4O_{12}$, this phenomenology gives rise to multiple spin-reorientation transitions driven by the competition of easy-axis single ion anisotropy and the Dzyaloshinskii-Moriya interaction; both within the manganese B-site sublattice. At low temperature one Er sublattice orders due to a finite f-d exchange field aligned parallel to its Ising axis, while the other Er sublattice remains non-magnetic until a final, symmetry-breaking phase transition into the ground state. This non-trivial low-temperature interplay of transition metal and rare-earth sublattices, as well as an observed $\mathbf{k} = (0, 0, 1/2)$ periodicity in both manganese spin canting and Er ordering, raises future challenges to develop a complete understanding of the $R_2CuMnMn_4O_{12}$ family.

1. Introduction

Spin-reorientation transitions are characterised by the spontaneous rotation of ordered magnetic moments [1], and have been found to occur in antiferromagnets [2–5], canted antiferromagnetics (weak ferromagnets) [6, 7], ferromagnets [8] and ferrimagnets [9, 10]. This phenomenon is of keen interest, not only from a fundamental perspective, but also because deterministic magnetization switching may be utilised in nanoscale functional spintronic components [11]. In this regard, spin-reorientation transitions in ferrimagnets are arguably the most appealing, as ferrimagnets carry a net magnetization while switching in the ultra-fast regime [12]. Spin-reorientation typically occurs due to competition between different magnetic sublattices with different magnetic anisotropies; a typical example is that of the rare-earth orthoferrites, in which spin-reorientation is driven by magnetic f-d exchange interactions between rare-earth and transition metal sublattices [6].

In quadruple perovskites, multiple magnetic sublattices may be introduced into the structure, allowing for complex frustrated exchange topologies and competing magnetic anisotropies. Indeed, many non-trivial magnetic phases have been observed in this structural family with properties including multiferroicity [13–15], low-field magnetoresistance [16], incommensurate magneto-structural coupling [17], and spin-reorientation transitions [9, 10]. The columnar quadruple perovskite $R_2CuMnMn_4O_{12}$ (R=Dy, Y) undergoes 3 magnetic phase transitions, two of which are spin-reorientation transitions involving the rotation of a ferrimagnetic magnetization by 90 degrees [10]. Remarkably, these transitions could not be explained by the conventional f-d exchange model, and it was proposed that these phenomena originated in the competition between single-ion anisotropy and anisotropy due to the Dzyaloshinskii-Moriya interaction, tuned by spin canting induced by frustrated Heisenberg exchange [10].

In this paper, we extend previous work on $R_2CuMnMn_4O_{12}$, and report the experimental characterization of the magnetic phases exhibited by $Er_2CuMnMn_4O_{12}$. The crystal structure of $Er_2CuMnMn_4O_{12}$ is shown in Figure 1. As is typical of perovskite-derived structures, the B site manganese ions are octahedrally coordinated forming a pseudo-cubic corner-sharing framework (Figure 1b and 1e). In the columnar perovskite aristotype (space group $P\frac{4_2}{n}mc$) [18,19], the MnO_6 octa-

hedra are severely tilted in an $a^+a^+c^-$ pattern (Glazer notation [20]). These octahedral tilts split the A sites into 3 symmetry inequivalent sublattices that are typically labelled A, A', and A'' (Figure 1a). The A sites are occupied by erbium, and sit within a distorted 10-fold oxygen coordination (Figure 1c). The A' sites are nominally occupied by copper (labelled Cu1) within a square-planar oxygen coordination, and the A'' sites are nominally occupied by manganese (labelled Mn2) within a tetrahedral oxygen coordination (Figure 1d).

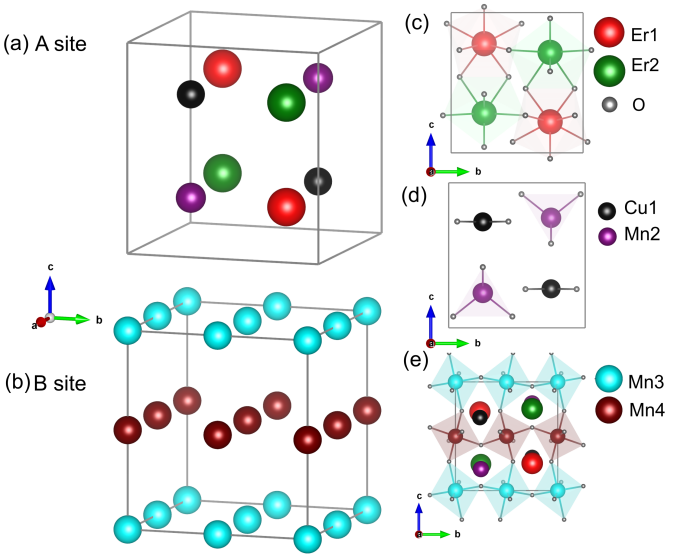

Figure 1
The crystal structure of $Er_2CuMnMn_4O_{12}$. A single unit cell is shown by thin grey lines, and the cation oxygen coordinations are shaded in panes c-e.

The $R_2CuMnMn_4O_{12}$ family also support layered charge and ferro-orbital ordering [21] that breaks the symmetry between nearest neighbor MnO_6 layers stacked along **c**, which we label Mn3 and Mn4, respectively. Mn3 ions carry a nominally 3+ oxidation state, and the cooperative Jahn-Teller distortions align $d_{3z^2-r^2}$ orbitals approximately parallel to **c**. The Mn4 ions are nominally 4+ and their octahedral coordination is undistorted to good approximation. A secondary consequence of the charge and orbital ordering is the splitting of the A sites into two sublattices, now related by a *pseudo*-4_2 screw, which we label Er1 and Er2. The space group of this distorted phase is *Pmmn*.

In this paper, we show that the complex interplay of the numerous magnetic sublattices described above leads to 4 magnetic phase transitions in $Er_2CuMnMn_4O_{12}$, characterized by the onset of ferrimagnetic order, spin-reorientation, spin-canting, and the polarisation of Er ions. The mechanism for spin-reorientation is likely the same as that proposed for other $R_2CuMnMn_4O_{12}$ compounds (R = Dy, Y), which show a similar sequence of phase transitions [10]. However, the nature of the observed low temperature coupling between rare-earth and transition metal sublattices in $Er_2CuMnMn_4O_{12}$, as well as the emergence of $\mathbf{k} = (0, 0, 1/2)$ modulations found at low temperature for R = Er, Dy, and Y, pose interesting questions for future studies.

The paper is organized as follows. In Section 2, we describe the experimental methods, and in Sections 3.1, 3.2, and 3.3 we present the results of magnetic susceptibility, specific heat, and neutron powder diffraction measurements, respectively. In Section 3.4, we find an approximate form for the Er crystal electric field using a simple point charge model, from which we successfully explain the empirical behavior of the Er ions at low temperature. Our results are discussed in Section 4, and finally, we draw conclusions in Section 5.

2. Experiment

A sample with the target chemical composition of $Er_{2.1}Cu_{0.95}Mn_{0.95}Mn_4O_{12}$ was prepared from a stoichiometric mixture of Er_2O_3, CuO, Mn_2O_3 and $MnO_{1.839}$ by a high-pressure, high-temperature method at 6 GPa and about 1650 K for 90 min in Pt capsules. The target chemical composition was slightly shifted from $Er_2CuMnMn_4O_{12}$ to eliminate the amount of a $ErCu_{3-x}Mn_{4+x}O_{12}$-type impurity, where magnetic susceptibility measurements showed that the magnetic properties of $Er_2CuMnMn_4O_{12}$ and $Er_{2.1}Cu_{0.95}Mn_{0.95}Mn_4O_{12}$ samples were almost identical except for a weak anomaly near 250 K from the impurity phase present in the $Er_2CuMnMn_4O_{12}$ sample. We note that neutron diffraction cannot distinguish between Er and Cu, and refinement of synchrotron X-ray diffraction data not shown here indicated that the tetrahedral Mn2 site accommodates the excess Er. For simplicity, we will use the chemical formula $Er_2CuMnMn_4O_{12}$ throughout the paper. AC magnetometry measurements were performed using a Quantum Design MPMS-1T with an excitation field of 0.5 Oe, on cooling in zero DC field from 225 to 2 K. The measurement was repeated for excitation frequencies of 2, 7, 110, 300, and 500 Hz. DC magnetometry measurements were performed using a Quantum Design MPMS-XL, having cooled the sample in zero magnetic field and measured on warming (ZFC), and measured in field on cooling (FCC), between 300 and 2 K in 100 Oe and between 400 and 2 K in 10 kOe fields. Specific heat data were collected using a Quantum Design PPMS on cooling in zero applied field, and in applied fields of 1, 2, 5, 10, 30, 50, and 70 kOe. Neutron powder diffraction measurements were performed using the WISH diffractometer [22] at ISIS, the UK Neutron and Muon Source. A 1.8 g sample was loaded into a 6 mm diameter vanadium can, and mounted within a ^{4}He cryostat. Data with high counting statistics (10 μA proton current at ISIS) were collected in each magnetic phase including paramagnetic for reference (1.5,9,30,140, and 200 K), and with lower counting statistics (4 μA proton current) on warming through the phases in finer temperature steps (3 -10 K intervals). Crystal and magnetic structure refinements were performed using the FULLPROF suite [23] against data collected in detector banks at average 2θ positions of 58.3° and 152.8°.

3. Results

3.1. Magnetic susceptibility

The temperature dependence of the real (χ') and imaginary (χ'') parts of the AC magnetic susceptibility are plotted in Figures 2a and 2b, respectively. Sharp anomalies in χ' indicate the

presence of 4 magnetic phase transitions at $T_{N1} \simeq 172$ K, $T_{N2} \simeq 115$ K, $T_{N3} \simeq 17$ K, and $T_{N4} \simeq 7$ K. We label the respective phases as CFI' ($T_{N2} \leq T \leq T_{N1}$), FI ($T_{N3} \leq T \leq T_{N2}$), CFI_1 ($T_{N4} \leq T \leq T_{N3}$), and CFI_2 ($T \leq T_{N4}$). These labels are consistent with those adopted in Reference [10] where CFI and FI refer to canted and non-canted ferrimagnetic phases, respectively. The prime denotes the high temperature CFI phase, while the numerical subscripts differentiate the two low temperature CFI phases. Anomalous behaviour at the phase transition temperatures is also seen in χ'', which shows a strong frequency dependence in the CFI' phase, indicative of non-trivial magnetic fluctuations.

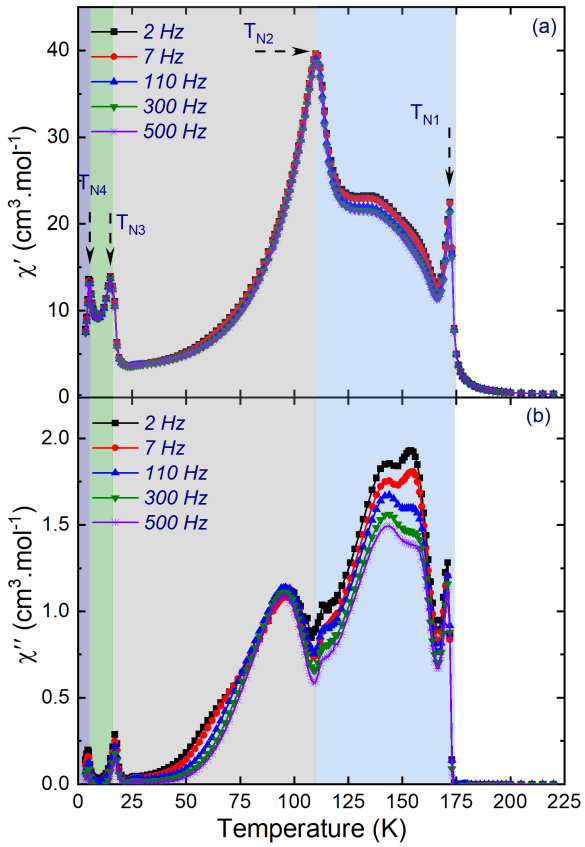

Figure 2
The real (a) and imaginary (b) parts of the AC magnetic susceptibility of $Er_2CuMnMn_4O_{12}$, measured as a function of temperature at different frequency 0.5 Oe excitation fields. The static DC field was zero. Four magnetic transitions are identified in (a), which bound phases CFI', FI, CFI_1, and CFI_2 shaded blue, grey, green and purple, respectively.

The DC magnetic susceptibility is shown in Figure 3a. Anomalies corroborate the phase transitions observed in the AC susceptibility data, described above. Furthermore, the sharp onset of magnetisation below T_{N1} shows that the CFI' phase is characterised by a significant ferromagnetic or ferrimagnetic moment, which is greatly reduced on cooling into the CFI_1 and CFI_2 phases. The broad anomaly at T_{N2} was also observed in $Dy_2CuMnMn_4O_{12}$ and $Y_2CuMnMn_4O_{12}$, where it was assigned to a softening of magnetic correlations in the proximity of a spin reorientation transition [10]. The inset to Figure 3a shows the inverse susceptibility against temperature. Fitting the Curie-Weiss model within the paramagnetic regime (in the temperature range 295 to 400 K) gave $\mu_{eff} = 15.40(4)\mu_B$/f.u. and $\theta_{CW} = 85(1)$ K. The positive value for θ_{CW} indicates dominant ferromagnetic interactions, and the effective moment is close to the theoretical value of $\mu = 17.3\mu_B$/f.u. (assuming $g = 2$ for transition metals).

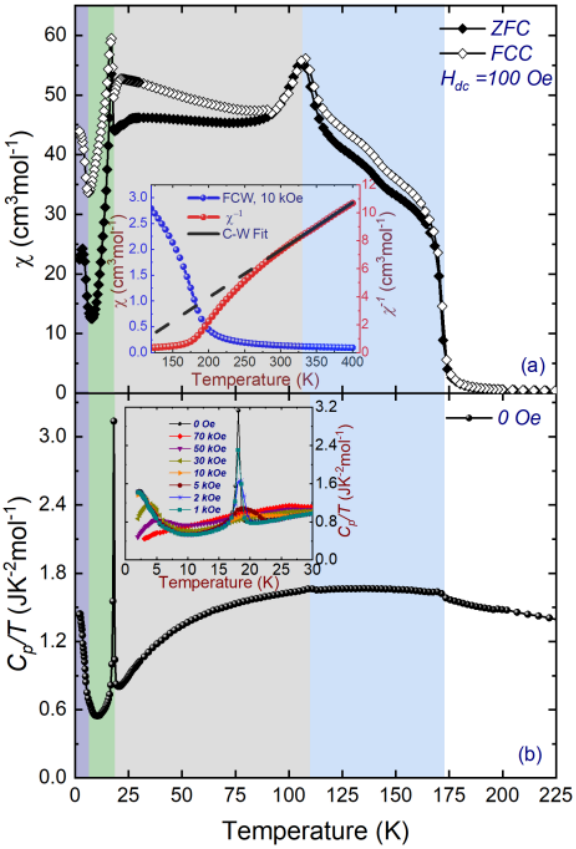

Figure 3
a) Temperature dependence of the DC magnetic susceptibility of $Er_2CuMnMn_4O_{12}$ measured under ZFC and FCC conditions in a 100 Oe applied field. The inset shows a Curie-Weiss fit (black dashed line) to the inverse susceptibility. b) Specific heat of $Er_2CuMnMn_4O_{12}$ measured as a function of temperature. The inset highlights the magnetic field dependence on the low temperature anomalies. Phases CFI', FI, CFI_1, and CFI_2 are shaded blue, grey, green and purple, respectively.

3.2. Specific heat

The temperature dependence of the specific heat is shown in Figure 3b. Clear anomalies are observed at each phase transition, with sharp peaks seen at T_{N3} and T_{N4}. We will later show that these transitions are associated with the ordering of Er^{3+} moments. Hence, these low temperature peaks in specific heat likely originate in the sequential splitting of Er^{3+} ground state doublets. Unfortunately, quantitative analysis of the entropy was not possible due to poor thermal conductivity from the pressed polycrystalline sample. However, the field dependent behaviour shown in the inset to Figure 3b is consistent with

a gradual, powder averaged field-induced splitting of the Er^{3+} ground state resulting in a 'smearing' of the peak in specific heat.

3.3. Neutron powder diffraction

The crystal structure of $Er_2CuMnMn_4O_{12}$ was refined against neutron powder diffraction data measured in the paramagnetic phase at 200 K. The structure of $Y_2CuMnMn_4O_{12}$ [10], with Y replaced by Er, was taken as a starting model. The crystal structure parameters are given in Table 1, and the fit to the data is shown in Figure 4a. Excellent agreement between model and data was achieved ($R = 4.58\%$, $wR = 3.28\%$, and $R_{\rm Bragg} = 6.0\%$).

Table 1

Crystal structure parameters of $Er_2CuMnMn_4O_{12}$(space group *Pmmn*) refined at 200 K. The lattice parameters were determined to be a = 7.2640(1) Å, b = 7.3187(1) Å, and c = 7.7764(1) Å. Atomic Wyckoff positions are Er1,Er2: 2a [1/4,1/4,z]; Cu1,Mn2: 2b [3/4,1/4,z]; Mn3: 4c [0,0,0]; Mn4: 4d [0,0,1/2]; O1: 8g [x,y,z]; O2,O4: 4f [x,1/4,z]; and O3,O5: 4e [1/4,y,z]. Bond valence sums (BVS) were calculated using the parameters, $R_0(Er^{3+}) = 1.99$, $R_0(Cu^{2+}) = 1.68$, $R_0(Mn^{2+}) = 1.79$, $R_0(Mn^{3+}) = 1.76$, $R_0(Mn^{4+}) = 1.75$, and $B = 0.37$, where the bond valence, $BV = \exp((R_o - R)/B)$. N.B. For mixed occupancy sites we give the BVS of the majority cation.

Atom	Frac. coord.	$U_{\rm iso}$ ($\times 10^{-2}$ Å^2)	BVS ($\|e\|$)	Occupation
Er1	z = 0.7785(6)	1.21(11)	+2.86	Er
Er2	z = 0.2834(6)	0.74(10)	+2.90	Er
Cu1	z = 0.7308(9)	0.98(2)	+1.98	76%Cu, 24% Mn
Mn2	z = 0.2410(6)	1.5(8)	+1.93	76%Mn, 24% Cu
Mn3	-	0.72(2)	+3.27	Mn
Mn4	-	0.45(2)	+3.74	Mn
O1	x = 0.4388(2) y = -0.0624(3) z = 0.2669(3)	0.90(7)	-	O
O2	x = 0.0587(4) z = 0.0413(3)	0.97(10)	-	O
O3	y = 0.5335(4) z = 0.9218(4)	0.59(9)	-	O
O4	x = 0.5343(4) z = 0.4188(4)	0.74(10)	-	O
O5	y = 0.4353(4) z = 0.5414(4)	0.82(9)	-	O

On cooling through $T_{\rm N1}$, new Bragg intensities appear in the neutron powder diffraction data (see Figure 4b). Given the coincidence with the magnetic susceptibility anomaly we can reasonably assume these new intensities originate in magnetic order. The magnetic peaks have a similar width to the nuclear peaks, indicating long-range magnetic correlations. The magnetic intensities appear in the same positions as nuclear intensities, and therefore index by the Γ-point propagation vector, $\mathbf{k} = (0, 0, 0)$. We refer the reader to the complete symmetry analysis of Γ-point magnetic structures in the *Pmmn* $R_2CuMnMn_4O_{12}$ columnar perovskites published in the Supplemental Material of Reference [10]. It was shown that the magnetic representation decomposes into 8 irreducible representations, of which only 4 allow for a net ferromagnetic moment observed in the DC magnetic susceptibility data; they are $m\Gamma_1^+$, $m\Gamma_2^+$, $m\Gamma_3^+$, and $m\Gamma_4^+$. Magnetic structure models also detailed in the Supplemental Material of Reference [10] constrained to each symmetry were systematically refined against the neutron powder diffraction data measured at 140 K, representative of phase CFI'. The only model compatible with the diffraction data was that transforming as $m\Gamma_4^+$. Within this symmetry, all magnetic sublattices (Er1, Er2, Cu1, Mn2, Mn3, and Mn4) can adopt ferromagnetic order polarised along $\pm\mathbf{b}$, with the addition of Mn3 and Mn4 antiferromagnetic A- and Y-type modes polarised along **a** and **c**, respectively [10]. The linear combination of ferromagnetic and antiferromagnetic modes leads to spin canting.

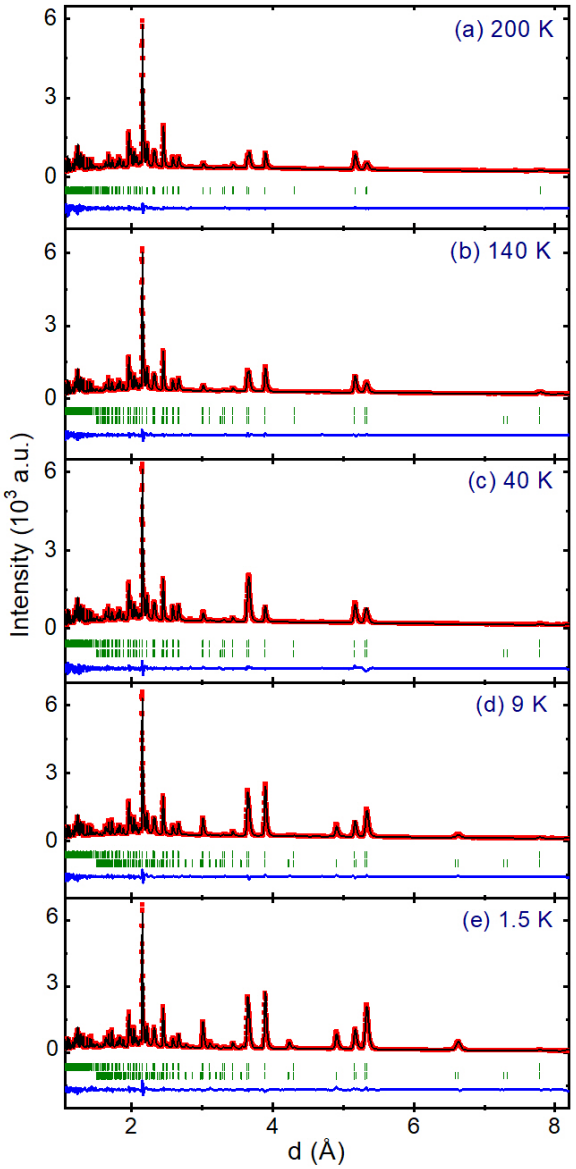

Figure 4
Neutron powder diffraction data measured in 5 phases; a) paramagnetic, b) CFI', c) FI, d) CFI_1, and e) CFI_2. Data are shown as red points, the fitted pattern as black lines, and the difference curve $I_{obs} - I_{calc}$ as a blue line at the bottom of the panes. The top and bottom row of green tick marks in each pane indicate the position of nuclear and magnetic Bragg peaks, respectively.

Our starting model had 10 free parameters (mode amplitudes), but after initial refinement the Er1, Er2, and Cu1 mode amplitudes could be set to zero. It is not surprising that the Er1 and Er2 moments are zero at this temperature, as A-site rare-earth ions in perovskite manganites typically order below low temperature phase transitions due to relatively weak *f-d* interactions. The absence of a moment at the Cu1 site is either due to the ordered moment being below the sensitivity of the diffraction experiment (approximately $< 0.1\mu_B$), or due to the mixed 76% Cu and 24% Mn cation occupation of that site refined against the paramagnetic data (see Table 1): If first we assume the random distribution of A'' Cu and Mn ions carry magnetic moments of 1 and 3 μ_B, respectively, and second, we assume the A'' Cu and Mn moments are aligned in opposite directions with respect to the nearest neighbour Mn3 and Mn4 sublattices due to opposite sign Cu-Mn and Mn-Mn A''-B exchange interactions, then the average moment at the Cu1 site is approximately zero.

Table 2
Magnetic structure parameters of $Er_2CuMnMn_4O_{12}$. The F and A labels denote ferromagnetic and Néel-type antiferromagnetic modes, respectively. The Y label denotes an Mn3/Mn4 mode of ferromagnetic stripes along **a**, coupled antiferromagnetically along **b** [10]. The subscripts indicate the polarisation of the modes. Freely refined and fixed values are given with and without standard uncertainties, respectively, and dashes indicate that the component is not allowed by the symmetry of the respective phase.

	$m\Gamma_2^+$	$m\Gamma_4^+$		mZ_4^+		mZ_3^+
Atom	F_z (μ_B)	F_y (μ_B)	A_x (μ_B)	A_x (μ_B)	Y_z (μ_B)	A_x (μ_B)
CFI' phase at 140 K						
Er1	-	0	-	-	-	-
Er2	-	0	-	-	-	-
Cu1	-	0	-	-	-	-
Mn2	-	-2.15(4)	-	-	-	-
Mn3	-	2.28(3)	0.19(2)	-	-	-
Mn4	-	1.31(3)	0	-	-	-
FI phase at 40 K						
Er1	0	-	-	-	-	-
Er2	0	-	-	-	-	-
Cu1	0	-	-	-	-	-
Mn2	-3.14(4)	-	-	-	-	-
Mn3	3.22(4)	-	-	-	-	-
Mn4	2.27(3)	-	-	-	-	-
CFI_1 phase at 9 K						
Er1	-	0	-	-	-	-
Er2	-	-5.02(4)	-	-	-	-
Cu1	-	0	-	-	-	-
Mn2	-	-3.23(6)	-	-	-	-
Mn3	-	1.91(3)	0	2.28(2)	0.93(3)	-
Mn4	-	2.70(3)	0	-	-	-
CFI_2 phase at 1.5 K						
Er1	-	0	-	0	-	-3.96(4)
Er2	-	-7.35(4)	-	0	-	0
Cu1	-	0	-	0	-	0
Mn2	-	-3.23	-	0	-	0
Mn3	-	1.91	0	2.28	0.93	-
Mn4	-	2.70	0	-	-	-

Further refinement indicated that the Y-type mode amplitudes should also be set to zero, while an additional A-type mode was required to properly account for the diffraction intensities. We note, however, that it was not possible to determine whether this mode resided on the Mn3 or Mn4 sublattice. Here, we propose a model in which spin canting occurs on the Mn3 sites — consistent with the low temperature structure. The final refinement of just 4 free parameters (given in Table 2) gave excellent agreement with the data ($R_{mag} = 2.00\%$). The refinement is shown in Figure 4b, and the evolution of the magnetic moment components as a function of temperature is shown in Figure 5. The magnetic space group for phase CFI' is $Pmm'n'$ (#59.410, basis=$\{[0,1,0],[-1,0,0],[0,0,1]\}$, origin=$[1/2, 1/2, 0]$, see supplementary mcif for full description).

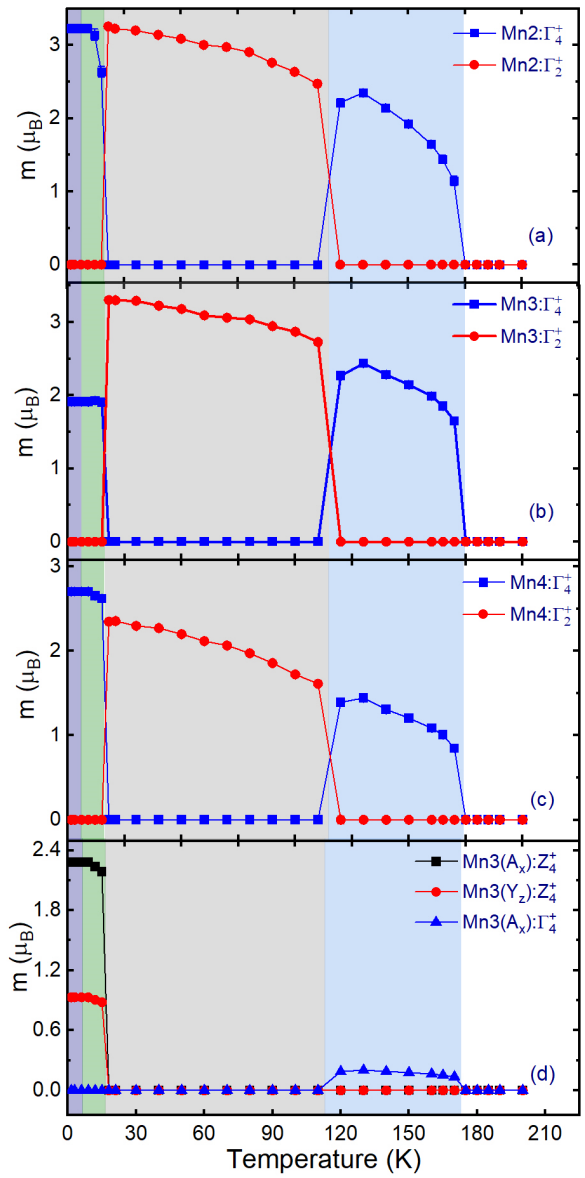

Figure 5
Temperature dependence of the $\pm F_i$ magnetic moments on the a) Mn2, b) Mn3, and c) Mn4 sublattices, where the blue and red data correspond to Γ_4^+ (F_y) and Γ_2^+ (F_z) order, respectively. Pane d shows the antiferromagnetic components that lead to spin canting on the Mn3 sublattice.

Cooling through T_{N2} gave rise to a redistribution of intensity amongst the Γ-point magnetic Bragg peaks consistent with a reorientation of the ferromagnetic modes from parallel to $\pm\mathbf{b}$, to parallel to $\pm\mathbf{c}$. Hence, the transition at T_{N2} is identified as a spin reorientation transition, from a structure transforming as $m\Gamma_4^+$ to one transforming as $m\Gamma_2^+$. The reoriented magnetic structure (maintaining zero moment on the Er1, Er2, and Cu1 sublattices) was refined against data measured at 40 K (see Figure 4c), an excellent fit was achieved ($R_{mag} = 1.98\%$), and the mode amplitudes are given in Table 2. We note that an A-type canting mode is not allowed within $m\Gamma_2^+$ symmetry, and other symmetry-allowed Mn3 and Mn4 canting modes were found to be zero. The magnetic space group for phase FI is $Pm'm'n$ (#59.409, basis=$\{[1,0,0],[0,1,0],[0,0,1]\}$, origin=$[1/2,1/2,0]$, see supplementary mcif for full description).

Below T_{N3} the Γ-point magnetic intensities change once more. Modelling of the diffraction pattern showed that the Mn2, Mn3, and Mn4 Γ-point magnetic structure returned to being polarised parallel to $\pm\mathbf{b}$. Furthermore, an additional ferromagnetic mode on the Er2 sublattice, also polarised parallel to $\pm\mathbf{b}$, was required to fully account for the Γ-point intensities (see Figure 6). This Er2 mode transformed by the same $m\Gamma_4^+$ irrep as the transition metal sublattices. Systematic tests against the data showed that no additional Γ-point modes appeared on any other sublattice, including Er1. The temperature dependence of the transition metal moments (Figure 5) showed that all moments approached saturation at the Γ-point, with the exception of the Mn3 sublattice, which showed a large drop in the Γ-point component through T_{N3}.

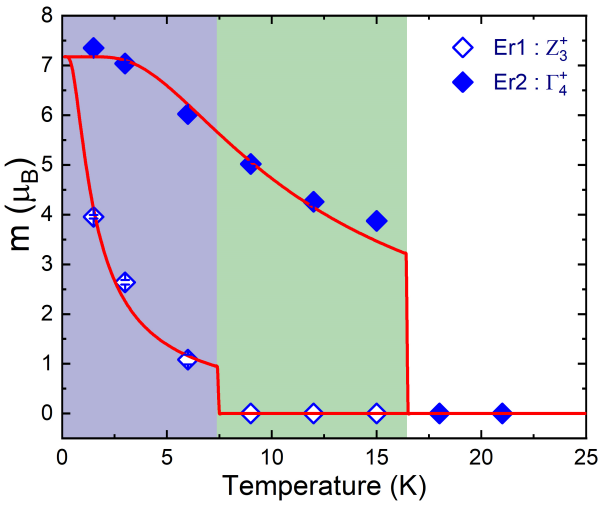

Figure 6
Temperature dependence of the Er1 and Er2 moments, whose respective magnetic modes transform a mZ_3^+ (antiferromagnetic, m||**a**), and $m\Gamma_4^+$ (ferromagnetic, m||**b**), respectively. Fits to a simple magnetisation model for a 2-level system are shown by red lines (see text for details).

In addition to the above changes, new diffraction peaks appeared below T_{N3}, which could be indexed with the Z-point propagation vector $\mathbf{k} = (0, 0, 1/2)$. Symmetry analysis reported in the Supplemental Material of reference [10] identified 8 possible Z-point symmetries. All were tested against the diffraction data, and it was found that the new Z-point intensities could be uniquely accounted for by A- and Y-type antiferromagnetic modes on the Mn3 sublattice, polarised along $\pm\mathbf{a}$ and $\pm\mathbf{c}$, respectively. These modes transform by the mZ_4^+ irrep, and correspond to a canting of the Mn3 moment, which, in any given layer, is similar to that found in phase CFI' albeit with a small additional Y mode. The main difference is that in the low temperature CFI_1 phase the relative sign of the canting alternates from one unit cell to the next along $\pm\mathbf{c}$ in accordance with the Z-point propagation vector. We note that this additional antiferromagnetic mode is consistent with

the observed reduction in the Mn3 moment at the Γ-point. A final refinement of the combined Γ-point and Z-point structures gave excellent agreement with the data ($R_{\rm mag}$ = 3.13%) as shown in Figure 4d, and the refined sublattice moments are given in Table 2. The magnetic space group for phase CFI_1 is $Pmm'n'$ (#59.410, basis=$\{[0,1,0],[-1,0,0],[0,0,2]\}$, origin=$[1/2,1/2,0]$, see supplementary mcif for full description).

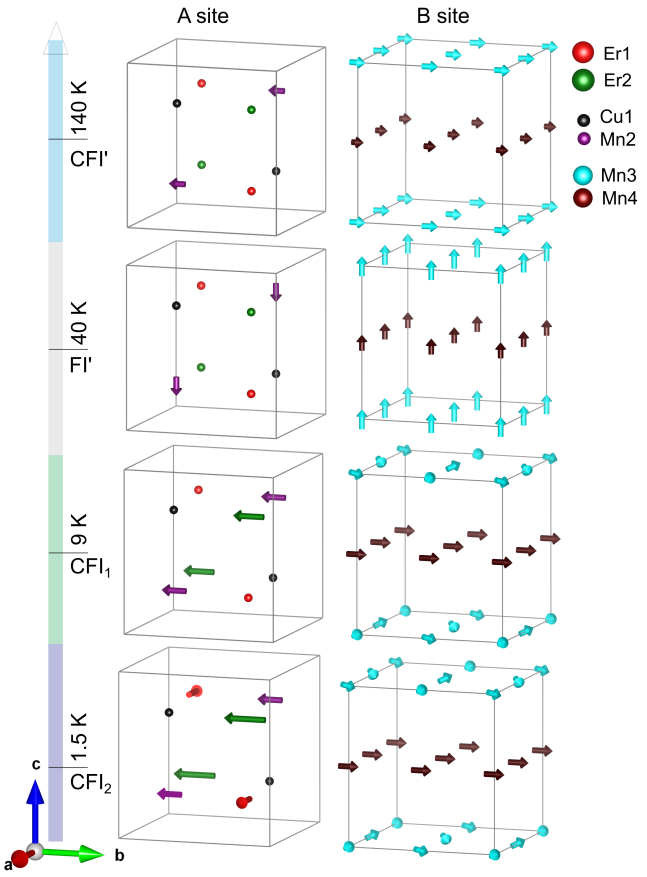

Figure 7
The magnetic structures of $Er_2CuMnMn_4O_{12}$in each ordered phase. Er1, Er2, Cu1, Mn2, Mn3, and Mn4 sublattices are coloured red, green, black, purple, cyan and maroon, respectively (see Figure 1).

Finally, below T_{N4} additional intensity appears at the Z-point Bragg peaks. Systematic tests of magnetic structures constrained by the CFI_1 phase magnetic symmetry (mZ_4^+) failed to account for this additional intensity, implying a symmetry breaking admixture of another Z-point irrep — consistent with the observation of a sharp phase transition. Expanding the magnetic structure tests to models transforming by all Z-point irreps, we identified an antiferromagnetic mode on the Er1 sublattice polarised parallel to ±**a** (perpendicular to Er2 moments), transforming as mZ_3^+, that uniquely accounted for the changes in neutron powder diffraction observed below T_{N2} (see Figure 6 for the temperature dependence of the Er moment). Unfortunately, peak overlap now led to excessive correlation between freely refining parameters, so it was necessary to fix the CFI_1 magnetic structure in refinements within the lower temperature CFI_2 phase. Still, excellent agreement with the data was achieved ($R_{\rm mag}$ = 3.82%, Figure 4e), and the parameters are summarised in Table 2. The magnetic space group for phase CFI_2 is $P2'/c'$ (#13.69, basis=$\{[-1,0,0],[0,0,2],[1,1,0]\}$, origin=$[1/2,1/2,0]$, see supplementary mcif for full description).

3.4. Er^{3+} crystal electric field

The site point symmetry of both Er ions is *mm*2, with pairs of Er1 and Er2 ions related by a *pseudo*-4_2 screw parallel to **c** (as present in the *P*4/*nmc* columnar perovskite aristotype [19]). Hunds rules gives J = 15/2 and g_J = 6/5 for the free Er^{3+} ion. In an orthorhombic *mm*2 crystal electric field (CEF), the degeneracy of states $|J,m_J\rangle$ will be lifted to 8 Kramers doublets. Assuming the energy gap between the ground state doublet and all others is $>> k_BT$, the magnetisation of a given Er ion in an effective f-d exchange field, $B_{\rm eff}$, will then be described by that of a two level system;

$$m = \mu.\tanh\left(\frac{\mu B_{\rm eff}}{k_BT}\right) \quad (1)$$

where μ is the available Er moment dependent on the ground state wavefunctions. The red lines in Figure 6 show fits of Equation 1 to the temperature dependence of the Er moments. The value of μ was constrained to be the same for both Er1 and Er2, and reasonable agreement is found for refined parameters $\mu = 7.2(1)\mu_B$, $B_{\rm eff}^{\rm Er1} = 0.20(2)$ T, and $B_{\rm eff}^{\rm Er2} = 1.6(1)$ T.

The ground state wavefunctions for Er1 and Er2 were estimated using a point charge model for the CEF. The Hamiltonian for a given Er ion is written

$$\mathcal{H} = \sum_n \sum_{m=-n}^{n} B_n^m O_n^m + g_J\mu_B \mathbf{J}\cdot\mathbf{B}_{\rm eff}, \quad (2)$$

The second term is the Zeeman energy, and the first term is the CEF energy, where O_n^m are Stevens operator equivalents [24] and the CEF parameters

$$B_n^m = A_n^m\langle r^n\rangle\Theta_n. \quad (3)$$

Here, Θ_n are the Stevens factors [24], $\langle r^n\rangle$ are radial expectation values for Er^{3+} [25], and in the point charge approximation

$$A_n^m = \frac{-|e|^2}{(2n+1)\epsilon_0} C_n^m \sum_i \frac{q_i}{r_i^{n+1}} Z_n^m(\theta_i,\phi_i). \quad (4)$$

The summation is taken over i nearest neighbour atoms of charge q_i and position (r_i,θ_i,ϕ_i). Z_n^m is a tesseral harmonic with numerical factor C_n^m, and ϵ_0 is the permittivity of free space. For each Er site, twelve oxygen ions were taken as nearest neighbours, with positions refined against the paramagnetic neutron powder diffraction data (described above). The calculated values of symmetry allowed B_n^m are given in Table 3.

Table 3
Crystal electric field parameters for Er1 and Er2 in units μeV (3.s.f.).

Atom	Crystal field parameters				
	B_2^0	B_2^2	B_4^0	B_4^2	B_4^4
Er1	340	-259	-0.138	-1.34	0.490
Er2	260	255	-0.0973	1.08	0.635
	B_6^0	B_6^2	B_6^4	B_6^6	
Er1	-0.00145	0.00703	0.0238	-0.0207	
Er2	-0.00148	-0.0111	0.0240	0.0226	

The CEF parameter magnitudes are similar for Er1 and Er2 with a sign change for B_2^2, B_4^2, B_6^2, and B_6^6, which is expected if they are related by *pseudo*-4_2 screw. The Hamiltonian was diagonalized for both Er ions, with small magnetic fields systematically applied parallel to **a**, **b**, and **c** to lift the doublet degeneracy. Evaluating the expectation value of the total angular momentum operators for the ground state wavefunctions showed that Er1 has a strong Ising-like single ion anisotropy parallel to **a**, and Er2 has a strong Ising-like single ion anisotropy parallel to **b**, in accordance with the empirical moment directions refined at low temperature.

4. Discussion

A similar sequence of phase transitions was observed in $R_2CuMnMn_4O_{12}$ (R = Y and Dy), where it was understood that frustrated Heisenberg exchange stabilised large spin canting (specifically the admixture of F and A modes) on the Mn3 sublattice in the CFI' and CFI phases. This spin canting introduced magnetic anisotropy via the Dzyaloshinskii-Moriya (DM) interaction, which could then compete with Mn3 single-ion-anisotropy (SIA). In $Y_2CuMnMn_4O_{12}$, this scenario provided a mechanism for both high and low temperature spin-reorientation transitions at T_{N2} and T_{N3}, even in the absence of f-d exchange. In $Dy_2CuMnMn_4O_{12}$, both phase transitions similarly occurred, but at T_{N3} the spin canting was not accompanied by spin-reorientation on account of the dominant Dy SIA parallel to **c** introduced via f-d exchange. In both R = Dy and Y compounds the low temperature spin canting was associated with a Z-point antiferromagnetic mode, as observed in the present study, and the origin of this doubled periodicity along **c** had not been explained [10].

The spin-reorientation transitions observed in $Er_2CuMnMn_4O_{12}$ at T_{N2} and T_{N3} can be explained by the same mechanism proposed for $Y_2CuMnMn_4O_{12}$. In addition, the Er2 moment becomes polarised below T_{N3} due to a finite f-d exchange field parallel to its Ising axis after spin-reorientation. To the contrary, the Er1 ions do not develop a moment at this temperature due to their Ising axis being perpendicular to the magnetization of the transition metal sublattice. Further, the Er1 Z-point symmetry-adapted mode for irrep mZ_4^+ is polarised along **b** [10], hence coupling to the mZ_4^+ Mn3 A mode is also prevented by the Er1 Ising anisotropy. Instead, the Er1 ions remain unpolarised, introducing a low temperature instability that leads to the symmetry breaking phase transition at T_{N4}. We find that below T_{N4}, the Er1 moments develop a finite polarisation parallel to their Ising axis, with their long-range order transforming by the mZ_3^+ irrep. This irrep is different to that of the Mn3 canting (mZ_4^+), which is consistent with the symmetry breaking transition but leads to questions regarding the nature of the coupling between Er1 and transition metal spins. We propose two possible scenarios. Firstly, that the transition at T_{N4} is magnetostructural (akin to a spin-Jahn-Teller transition [26]) whereby a spontaneous symmetry-breaking structural distortion facilitates coupling between the mZ_3^+ A mode at the Er1 sublattice and the mZ_4^+ A mode at the Mn3 sublattice. Secondly, the Mn3 canting may adopt an additional mZ_3^+ mode, which then couples directly to the Er1 sublattice. In the former case the primary energy cost associated with the transition is elastic, while in the latter case the primary energy cost is in magnetic exchange.

Finally, we note that the above behaviour is consistent with the refined parameters of our two level system fitted to the Er1 and Er2 moment temperature dependencies. Both Er1 and Er2 can develop the same size moment in the ground state (below the base temperature of the neutron powder diffraction experiment), but the Er1 moment reduces rapidly on warming due to the weaker f-d exchange field while the Er2 moment is sustained to higher temperatures by a larger field. This is consistent with the sequence of phase transitions, and exactly what one would expect if the Er1 moment is coupled to an antiferromagnetic mode of the single Mn3 sublattice while the Er2 moment is coupled to multiple ferromagnetic sublattices.

5. Conclusions

In summary, we have shown that $Er_2CuMnMn_4O_{12}$ undergoes 4 magnetic phase transitions. Below $T_{N1} \simeq 172$ K, the system adopts ferrimagnetic order of transition metal ions polarized along $\pm$**b**, with antiferromagnetic canting on the Mn3 B site sublattice. A spin-reorientation transition occurs at $T_{N2} \simeq 115$ K, where the ferrimagnetic order rotates to be polarized along $\pm$**c**. The antiferromagnetic canting vanishes in this phase in accordance with magnetic symmetry. A second spin-reorientation transition occurs at $T_{N3} \simeq 17$ K, where the ferrimagnetic order returns to $\pm$**b**. Mn3 sublattice antiferromagnetic canting also reappears at T_{N3}, but now with a doubled periodicity along **c** ($\mathbf{k} = (0, 0, 1/2)$). Furthermore, the transition metal ferrimagnetic order is now accompanied by a moment at the Er2 sublattice, which has an Ising axis parallel to the ferrimagnetic magnetization. To the contrary, the Er1 sublattice remains non-magnetic in this phase as its Ising axis is perpendicular to the ferrimagnetic magnetization. As a result, a fourth and final symmetry-breaking phase transition occurs at $T_{N4} \simeq 7$ K characterized by the $\mathbf{k} = (0, 0, 1/2)$ ordering of the Er1 moments that couple to the pre-existing antiferromagnetic spin canting of the Mn3 sublattice. The mechanism for spin-reorientation is likely the same as that proposed for other $R_2CuMnMn_4O_{12}$ compounds, which show a similar sequence of phase transitions [10]. However, the nature of the low temperature coupling between Er1 and Mn3 sublattices is not clear from our elastic diffraction data or symmetry analysis. We have proposed two scenarios based on elastic and magnetic energies, and it would be interesting to differentiate these two mechanisms in future

studies. Furthermore, the origin of the $\mathbf{k} = (0, 0, 1/2)$ modulation in $Er_2CuMnMn_4O_{12}$, and other $R_2CuMnMn_4O_{12}$ compounds (R = Y, Dy), is currently unknown, presumably originating in subtleties of the exchange topology in this complex, multi-sublattice system.

Acknowledgements J.M.A-B. would like to thank the Coordenação de Aperfeiçoamento de Pessoal de Nível Superior (CAPES) and the PDSE - Programa de Doutorado Sanduíche no Exterior (Processo: PDSE - 88881.846711/2023-01) for funding a visiting scholarship.

References

[1] H. Horner and C. M. Varma. Nature of spin-reorientation transitions. *Phys. Rev. Lett.*, 20:845–846, 1968.

[2] S. A. J. Kimber, A. H. Hill, Y-Z. Zhang, H. O. Jeschke, R. Valentí, C. Ritter, I. Schellenberg, W. Hermes, R. Pöttgen, and D. N. Argyriou. Local moments and symmetry breaking in metallic PrMnSbO. *Phys. Rev. B*, 82:100412, 2010.

[3] A. Marcinkova, T. C. Hansen, C. Curfs, S. Margadonna, and J. W. G. Bos. Nd-induced Mn spin-reorientation transition in NdMnAsO. *Phys. Rev. B*, 82:174438, 2010.

[4] Q. Zhang, W. Tian, S. G. Peterson, K. W. Dennis, and D. Vaknin. Spin reorientation and Ce-Mn coupling in antiferromagnetic oxypnictide CeMnAsO. *Phys. Rev. B*, 91:064418, 2015.

[5] A. J. Corkett, D. G. Free, and S. J. Clarke. Spin-reorientation transition in CeMnAsO. *Inorganic Chemistry*, 54(3):1178–1184, 2015.

[6] R. L. White. Review of Recent Work on the Magnetic and Spectroscopic Properties of the Rare-Earth Orthoferrites. *Journal of Applied Physics*, 40(3):1061–1069, 1969.

[7] J. P. Bolletta, F. Pomiro, R. D. Sánchez, V. Pomjakushin, G. Aurelio, A. Maignan, C. Martin, and R. E. Carbonio. Spin reorientation and metamagnetic transitions in RFe$_{0.5}$Cr$_{0.5}$O$_3$ perovskites (R = Tb, R = Dy, R = Ho, R = Er). *Phys. Rev. B*, 98:134417, 2018.

[8] Z. Tie-son, J. Han-min, G. Guang-hua, H. Xiu-feng, and C. Hong. Magnetic properties of R ions in RCo$_5$ compounds (R = Pr, Nd, Sm, Gd, Tb, Dy, Ho, and Er). *Phys. Rev. B*, 43:8593–8598, 1991.

[9] A. M. Vibhakar, D. D. Khalyavin, P. Manuel, L. Zhang, K. Yamaura, P. G. Radaelli, A. A. Belik, and R. D. Johnson. Magnetic structure and spin-flop transition in the *a*-site columnar-ordered quadruple perovskite TmMn$_3$O$_6$. *Phys. Rev. B*, 99:104424, 2019.

[10] A. M. Vibhakar, D. D. Khalyavin, P. Manuel, J. Liu, A. A. Belik, and R. D. Johnson. Spontaneous rotation of ferrimagnetism driven by antiferromagnetic spin canting. *Phys. Rev. Lett.*, 124:127201, 2020.

[11] N. Locatelli, V. Cros, and J. Grollier. Spin-torque building blocks. *Nature Materials*, 13:11–20, 2014.

[12] Y. Yang, R.B. Wilson, J. Gorchon, C.-H. Lambert, S. Salahuddin, and J. Bokor. Ultrafast magnetization reversal by picosecond electrical pulses. *Nature Materials*, 3:e1603117, 2017.

[13] F. Mezzadri, G. Calestani, M. Calicchio, E. Gilioli, F. Bolzoni, R. Cabassi, M. Marezio, and A. Migliori. Synthesis and characterization of multiferroic BiMn$_7$O$_{12}$. *Phys. Rev. B*, 79:100106, 2009.

[14] R. D. Johnson, L. C. Chapon, D. D. Khalyavin, P. Manuel, P. G. Radaelli, and C. Martin. Giant improper ferroelectricity in the ferroaxial magnet CaMn$_7$O$_{12}$. *Phys. Rev. Lett.*, 108:067201, 2012.

[15] D. Behr, A. A. Belik, D. D. Khalyavin, and R. D. Johnson. BiMn$_7$O$_{12}$: Polar antiferromagnetism by inverse exchange striction. *Phys. Rev. B*, 107:L140402, 2023.

[16] Z. Zeng, M. Greenblatt, M. A. Subramanian, and M. Croft. Large low-field magnetoresistance in perovskite-type CaCu$_3$Mn$_4$O$_{12}$ without double exchange. *Phys. Rev. Lett.*, 82:3164–3167, 1999.

[17] R. D. Johnson, D. D. Khalyavin, P. Manuel, A. Bombardi, C. Martin, L. C. Chapon, and P. G. Radaelli. Modulated spin helicity stabilized by incommensurate orbital density waves in a quadruple perovskite manganite. *Phys. Rev. B*, 93:180403, 2016.

[18] G. King and P. M. Woodward. Cation ordering in perovskites. *J. Mater. Chem.*, 20:5785–5796, 2010.

[19] A. A. Belik. Rise of A-site columnar-ordered $A_2A'A''B_4O_{12}$ quadruple perovskites with intrinsic triple order. *Dalton Trans.*, 47:3209–3217, 2018.

[20] A. M. Glazer. The classification of tilted octahedra in perovskites. *Acta Crystallographica Section B*, 28(11):3384–3392, 1972.

[21] A. A. Belik, D. D. Khalyavin, L. Zhang, Y. Matsushita, Y. Katsuya, M. Tanaka, R. D. Johnson, and K. Yamaura. Intrinsic triple order in *A*-site columnar-ordered quadruple perovskites: Proof of concept. *ChemPhysChem*, 19(19):2449–2452, 2018.

[22] L. C. Chapon, P. Manuel, P. G. Radaelli, C. Benson, L. Perrott, S. Ansell, N. J. Rhodes, D. Raspino, D. Duxbury, E. Spill, and J. Norris. Wish: The new powder and single crystal magnetic diffractometer on the second target station. *Neutron News*, 22(2):22–25, 2011.

[23] J. Rodríguez-Carvajal. Recent advances in magnetic structure determination by neutron powder diffraction. *Physica B: Condensed Matter*, 192(1):55–69, 1993.

[24] M. Hutchings. *Solid State Physics*, 16:227, 1964.

[25] A.J. Freeman and J.P. Desclaux. Dirac-Fock studies of some electronic properties of rare-earth ions. *Journal of Magnetism and Magnetic Materials*, 12(1):11–21, 1979.

[26] F. K. K. Kirschner, R. D. Johnson, F. Lang, D. D. Khalyavin, P. Manuel, T. Lancaster, D. Prabhakaran, and S. J. Blundell. Spin jahn-teller antiferromagnetism in CoTi$_2$O$_5$. *Phys. Rev. B*, 99:064403, 2019.